Matter and Radiation at Extremes

RESEARCH ARTICLE

pubs.aip.org/aip/mre

Study of the spatial growth of stimulated Brillouin scattering in a gas-filled hohlraum via detecting the driven ion acoustic wave

Cite as: Matter Radiat. Extremes 9, 027601 (2024); doi: 10.1063/5.0173023
Submitted: 19 August 2023 • Accepted: 30 November 2023 •
Published Online: 2 January 2024

Chaoxin Chen,[1] Tao Gong,[1,a)] Zhichao Li,[1] Liang Hao,[2] Yonggang Liu,[1] Xiangming Liu,[1] Hang Zhao,[1] Yaoyuan Liu,[1] Kaiqiang Pan,[1] Qi Li,[1] Sanwei Li,[1] Zhijun Li,[1] Sai Jin,[1] Feng Wang,[1,b)] and Dong Yang[1]

AFFILIATIONS

[1] Laser Fusion Research Center, China Academy of Engineering Physics, Mianyang, Sichuan 621900, People's Republic of China
[2] Institute of Applied Physics and Computational Mathematics, Beijing 100094, People's Republic of China

[a)] **Author to whom correspondence should be addressed:** gongtao_lfrc@163.com
[b)] **Electronic mail:** wangfeng7566@163.com

ABSTRACT

In an experiment performed on the Shenguang-III prototype laser facility, collective Thomson scattering (TS) is used to study the spatial growth of stimulated Brillouin scattering (SBS) in a gas-filled hohlraum by detecting the SBS-driven ion acoustic wave. High-quality time-resolved SBS and TS spectra are obtained simultaneously in the experiment, and these are analyzed by a steady-state code based on the ray-tracing model. The analysis indicates that ion–ion collisions may play an important role in suppressing SBS growth in the Au plasma; as a result, the SBS excited in the filled gas region is dominant. In the early phase of the laser pulse, SBS originates primarily from the high-density plasma at the edges of the interaction beam channel, which is piled up by the heating of the interaction beam. Throughout the duration of the laser pulse, the presence of the TS probe beam might mitigate SBS by perturbing the density distribution around the region overlapping with the interaction beam.

I. INTRODUCTION

In indirect-drive inertial confinement fusion (ICF), a millimeter-scale Au/U hohlraum filled with low-Z gas is used to convert laser energy into x rays, which uniformly irradiate a DT capsule that is placed at the hohlraum center.[1] It was realized at the very beginning that laser plasma instabilities (LPIs)[2] could be detrimental to the energy coupling from lasers to the hohlraum. For example, in low-gas-filled (0.3 mg/cm^3) hohlraums, stimulated Brillouin scattering (SBS) is of great concern.[3] This is because the scattered light can not only take energy away from the pump laser,[4,5] but also potentially damage the optical components,[6] thereby limiting the maximum output energy of the laser facility. Although a controlled fusion experiment exceeding the Lawson criterion has been achieved on the National Ignition Facility (NIF) with a low-gas-filled hohlraum,[7] the laser power of the outer beams are ramped down at the end of the pulse, to avoid strong SBS.[5,8] For achieving high-gain fusion in the future, longer laser pulses and higher-gas-filled hohlraums are required, which will inevitably lead to strong SBS.[9–11] Therefore, studying SBS in a high-gas-filled hohlraum is still important for indirect-drive ICF research.

To study SBS under ICF conditions, a large number of experiments have been performed.[12] Gas bag targets have been used to study SBS in the filled gas region, and it has been found that SBS reflectivity saturates at the 30% level for laser intensities above 5×10^{14} W/cm^2.[13] Experiments with direct measurement of SBS light from ICF hohlraums have also been performed at different laser facilities, such as the Omega laser facility,[14] the NIF,[15] and the Shenguang laser facilities.[16] These experiments have investigated in detail the factors influencing SBS in hohlraums, such as target geometry,[14] gas fill,[4] and laser smoothing techniques.[16] However, given that the distribution of plasma parameters along the laser path inside an ICF hohlraum is quite complex, it is very difficult to determine the exact excitation region of SBS simply from the detected scattered light. To analyze the spatial growth of SBS,

steady-state models have been developed to enable rapid calculations of the scattered light based on the plasma parameters provided by radiation-hydrodynamics simulations.[17,18] These models have revealed some important mechanisms impacting on LPI, such as competition between SBS and stimulated Raman scattering (SRS),[19] plasma heating via external magnetic fields[20] and mixing between the filled gas and Au plasma from the hohlraum wall.[21] Nonetheless, when these models were applied to the complex conditions in ICF hohlraums, discrepancies were found between calculations and experiments. For example, in our previous studies of SBS on the Shenguang-III prototype laser facility (SG-IIIp), the calculated SBS spectra always contained an extra component originating from the Au plasma, which was not observed in the experimental data.[18] One of the possible explanations for this is that the neglect of ion–ion collisions in the calculation led to overestimation of the contribution of SBS in the Au plasma. However, this speculation has yet to be validated.

One way to experimentally study the spatial growth of SBS is to use collective Thomson scattering (TS)[22] to diagnose the ion acoustic wave (IAW) driven by SBS locally.[13] The TS diagnostic has been widely used in experiments with an open configuration (e.g., plate targets and gas bag targets), which have verified saturation mechanisms of SBS, such as ion trapping,[23] detuning by the velocity gradient,[24] and two-ion decay.[25] However, owing to the requirement of a rigorous geometric relation between the SBS-driven IAW (determined by the pump laser), the TS probe beam, and the diagnostic system,[26] TS has seldom been applied to experiments with a closed configuration, such as that of an ICF hohlraum target.

Taking advantage of a recently developed large-aperture TS diagnostic system,[26] we apply TS to an ICF gas-filled hohlraum for the first time (to the best of our knowledge) to detect the driven IAW, so as to study the spatial growth of SBS. The results indicate that SBS primarily consists of two components, occurring respectively in the early and late phases of the laser pulse, both of which are primarily from the filled gas (CH) plasma. At early times, laser heating increases the electron density at the edges of laser channel, scattering high-intensity SBS light. At late times, the flow velocity in the hohlraum is relatively uniform, and hence produces strong SBS light. Owing to ion–ion collisional damping and the small size of the high-Z (Au) wall plasma, SBS in the wall plasma is weak. The additional TS probe beam in the experiment may suppress SBS, because of its perturbation of the local density distribution. These findings have improved the understanding of SBS in gas-filled hohlraums and may play an important role in mitigating SBS in the future experiments.

The remainder of the paper is organized as follows. In Sec. II, we introduce the experimental setup and results. In Sec. III, we present the plasma parameters provided by radiation-hydrodynamics simulation. In Sec. IV, we introduce the models for SBS and TS calculations. In Sec. V, we analyze the factors affecting SBS in gas-filled hohlraums, including ion–ion collisions and transverse density variations caused by the interaction beam and the TS probe beam. Section VI provides a brief summary.

II. EXPERIMENTAL SETUP AND RESULTS

The experiment is conducted on the Shenguang-III prototype laser facility (SG-IIIp), as shown in Fig. 1. The target is a cylindrical

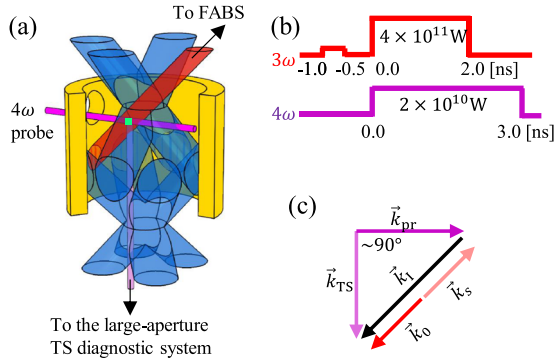

FIG. 1. (a) Experimental setup, with nine laser beams injected into a cylindrical gas-filled Au hohlraum. The blue beams are 3ω heaters. The red beam is the 3ω interaction beam. The purple and lilac beams are the 4ω TS probe beam and the TS light, respectively. The green square is the TS diagnostic volume. (b) Relative timings of 3ω beams and the 4ω beam. (c) Diagram detailing the ion-acoustic wave vector probed. Here, $\vec{k}_0$, $\vec{k}_s$, and $\vec{k}_I$ are the wave vectors of the interaction beam, the SBS light, and the SBS-driven IAW, respectively.

Au hohlraum [see Fig. 1(a)] with a diameter of 1.4 mm and a length of 1.4 mm, and the open ends of the hohlraum serve as laser entrance holes (LEHs). The hohlraum is filled with pentane (C_5H_{12}) gas at a pressure of 0.6 atm, corresponding to an electron density of 6.3×10^{20} cm^{-3} when fully ionized. The 1500 mg/cm^3, 0.5 μm-thick polyimide covering membrane for gas filling is not shown. There is a 400 μm-diameter diagnostic hole on the wall of the hohlraum for injection of the TS probe beam. As shown in

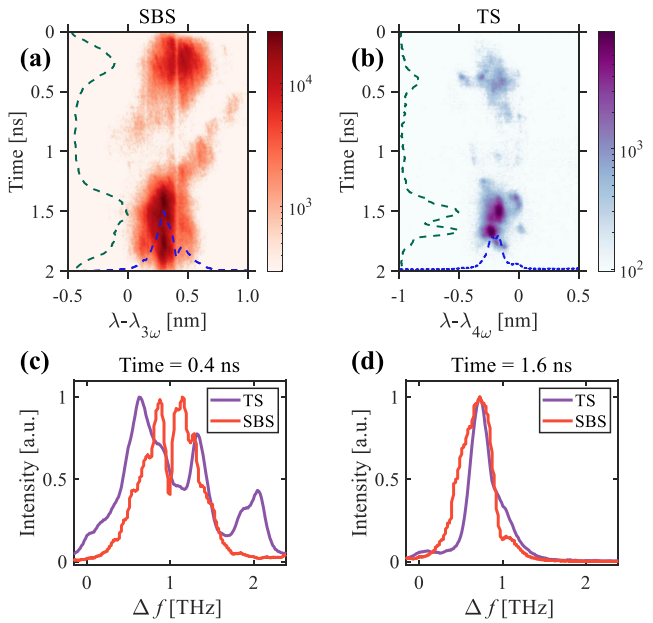

FIG. 2. (a) Time-resolved spectrum of SBS light from the interaction beam. (b) Time-resolved spectrum of the TS light off the SBS-driven IAW in the diagnostic volume shown in Fig. 1(a). Frequency shifts of SBS light and TS light respectively relative to the interaction beam and the probe beam at (c) 0.4 ns and (d) 1.6 ns.

Fig. 1(a), eight 3ω (351 nm) beams enter the hohlraum through both ends, with an angle of 45° relative to the hohlraum axis, irradiating 200 μm below its waist. Each 3ω beam delivers an energy of 800 J in a 2 ns main pulse plus a 0.5 ns pre-pulse [see Fig. 1(b)]. All 3ω beams are smoothed by continuous phase plates (CPPs) and focused by $f/5.4$ lenses. Seven of them are used as heater beams and the other as an interaction beam. The heater beams are focused on the LEH plane, forming 500 μm-diameter focal spots. To drive strong SBS, the interaction beam forms a smaller focal spot with a diameter of 300 μm, which corresponds to an average intensity of $\sim 8 \times 10^{14}$ W/cm^2. The energy and spectrum of the backscattered SBS light are diagnosed by a full-aperture backscattering station (FABS). The SBS-driven IAW with a wave vector ($\vec{k}_I = \vec{k}_0 - \vec{k}_s \approx 2\vec{k}_0$) [see Fig. 1(c)] is detected by a 4ω (263.3 nm) TS probe beam. Routinely, the probe beam is synchronized with the main pulse of the 3ω beams, delivering 60 J energy in a 3 ns-square pulse. The probe beam is focused to a 70 μm-diameter spot by an $f/7$ lens. The TS light is collected by a large aperture ($f/3$) TS diagnostic system. The probe beam and the TS diagnostic system define a diagnostic volume ($\phi 70 \times 100$ μm^2), which is located at the center of the interaction beam, 400 μm from the upper LEH and 200 μm from the hohlraum axis, as shown by the green square in Fig. 1(a).

Figures 2(a) and 2(b) show the time-resolved spectra of the SBS light and the TS light off the SBS-driven IAW in the diagnostic volume shown in Fig. 1(a), respectively. The SBS reflectivity is about 4%. The SBS light consists of two components with comparable intensities, one in the early phase (0–0.7 ns) and the other in the late phase (1.2–1.9 ns) of the laser pulse. The TS light also contains two components similar to SBS light. TS light characterizes the SBS-driven IAW in the diagnostic volume, which correlates with the SBS light therein. Compared with the SBS spectrum, the two components of the TS spectrum have a greater contrast, with a much weaker signal in the early phase, which could come from two possible causes. One is that early SBS light primarily grows around the LEH, which

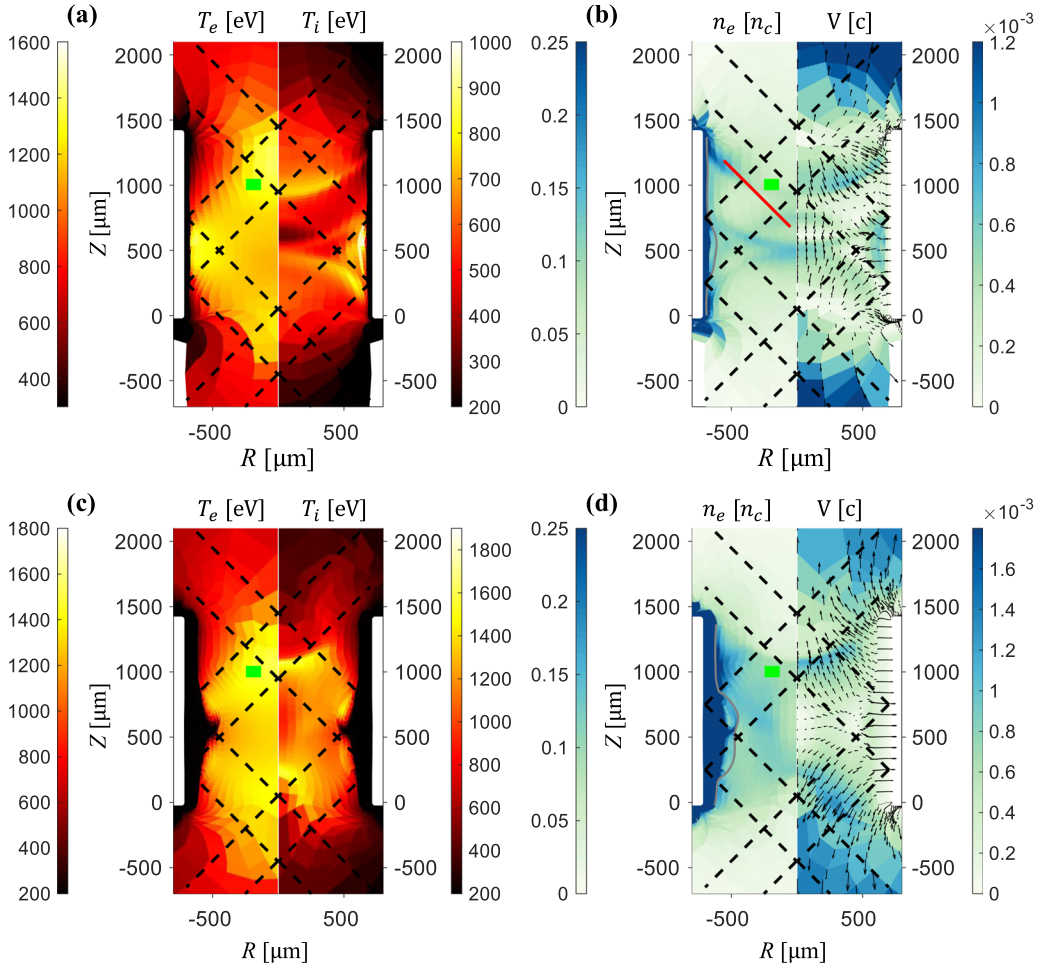

FIG. 3. Simulated spatial distributions of plasma parameters at 0.4 ns [(a) and (b)] and 1.6 ns [(c) and (d)]. The black dashed lines show the boundaries of heater beams with diameters of 500 μm in the R direction. The gray lines at the left of (b) and (d) are the interfaces between the Au and CH plasmas. The electron density along the red line in (b) is shown in Fig. 4. The green square is the TS diagnostic volume. Here, n_c is the critical density of the 3ω laser, $n_c \approx 9 \times 10^{21}$ cm^{-3}.

is behind the TS diagnostic volume. The other is that SBS mainly occurs at the edge of the interaction beam, which the TS diagnostic volume does not cover.

The frequency shift of the TS spectrum relative to the probe beam is generally the same as that of the SBS spectrum relative to the interaction beam [see Figs. 2(c) and 2(d)], which demonstrates that the IAW detected by the TS diagnostic is indeed driven by the interaction beam and the SBS light. However, there are some minor differences between the two spectra. For example, at 0.4 ns, the SBS spectrum (0.4–1.6 THz) is narrower than the TS spectrum (0.1–2.2 THz), as shown in Fig. 2(c). A reasonable explanation is that the central part of the SBS spectrum experiences stronger amplification in the region from the TS diagnostic volume to the LEH, owing to its better coupling with the plasma parameters therein. The widths of the late (1.6 ns) SBS and TS spectra [see Fig. 2(d)] are both much narrower than the corresponding early spectra [see Fig. 2(c)], implying that the plasma parameters are more homogeneous in the late phase.

III. RADIATION-HYDRODYNAMICS SIMULATION

To obtain plasma parameters for SBS analysis, a 2D cylindrically symmetric radiation-hydrodynamics simulation for the SG-IIIp gas-filled hohlraum is performed using the code LARED.[27] This code has already been benchmarked in an almost identical experiment, by comparing the simulated plasma parameters inside the hohlraum with those measured by TS.[28] Restricted by the cylindrical symmetry, the diagnostic hole and the probe beam are absent in the simulation, and all 3ω lasers, including the interaction beam, have the same focal spots with diameters of 500 μm in the R direction. The 0.5 μm-thick covering membrane used in the experiment is too thin to be simulated, and so it is replaced by a mass-equivalent membrane with a greater thickness (50 μm) and a lower density 15 mg/cm^3. As will be shown below, these differences between the experiment and the simulation cannot be ignored in the SBS analysis.

Figure 3 shows the spatial distributions of the simulated plasma parameters for two typical times: 0.4 and 1.6 ns. Owing to the laser heating, the plasma temperature inside the laser channel is higher than that outside, while the electron density inside is lower than that outside, as shown by the profile at 0.4 ns (red line) in Fig. 4. This is because at early times, the transverse pressure caused by laser heating pushes the initially static plasma out from the laser channel, resulting in a low density at the center and a high density at the edges. As the heating continues, the transverse electron density distribution around the channel becomes flat, as shown by the blue line in Fig. 4. The density increase at the channel center at 0.7 ns is due to the expansion of the Au bubble, which compresses the CH plasma inside the hohlraum.

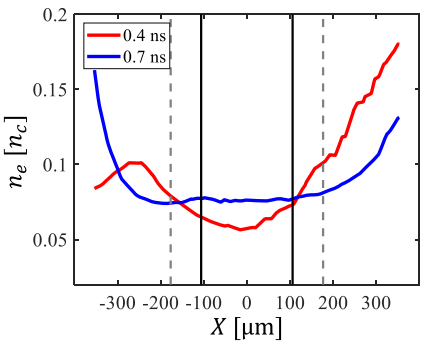

FIG. 4. Electron density profiles across the 3ω laser as marked by the red line in Fig. 3(b). The black lines are the boundaries of interaction beam. The dashed gray lines are the boundaries of the heater beam.

IV. MODELS FOR CALCULATING SBS AND TS

Based on the plasma parameters from the LARED simulation, we calculate the SBS light of different rays in the interaction beam using the 1D steady-state model from Ref. 19. The total SBS light of the interaction beam is then obtained by summing the scattered light of these rays. Specifically, along each ray in the 300 μm-diameter interaction beam, the model solves

$$\mathrm{d}_l I_0(l) = -\kappa_0 I_0 - I_0 \int \mathrm{d}\omega_s \frac{\omega_0}{\omega_s}(\tau_1 + \Gamma i_s), \tag{1}$$

$$-\partial_l i_s(l,\omega_s) = -\kappa_s i_s + \Sigma + I_0(\tau_1 + \Gamma i_s). \tag{2}$$

Here, l is the distance along the ray of the interaction (pump) beam. ω_0 and I_0 are respectively the frequency and intensity of the interaction beam. It should be noted that although the average intensity of the interaction beam in experiment is ~8×10^{14} W/cm^2, a value of $I_0 = 2 \times 10^{15}$ W/cm^2 is used in SBS calculations for considering the high-intensity speckles in the focal spot.[16] $i_s\ \mathrm{d}\omega_s$ is the intensity of the SBS light within the frequency interval between ω_s and $\omega_s + \mathrm{d}\omega_s$. κ_0 and κ_s are the inverse bremsstrahlung absorption coefficients of the interaction beam and the SBS light, respectively. $I_0\tau_1$ represents the noise source from TS and Σ the noise source from bremsstrahlung. The absorption coefficients and noise sources are basically the same as those used in Ref. 17, except that the effects of whole-beam focusing are omitted. The coupling coefficient Γ is expressed as

$$\Gamma = -\frac{k_I^2 e^2}{m_e^2 c^2}\frac{2\pi}{k_s k_0 \omega_0}\mathrm{Im}\left[\frac{\chi_e(1+\chi_i)}{\varepsilon}\right], \tag{3}$$

where e and m_e are respectively the charge and mass of the electron, and k_I is the wavenumber of the SBS-driven IAW. χ_e and χ_i are the collisionless electron and ion susceptibilities, respectively. $\varepsilon = 1 + \chi_e + \chi_i$ is the plasma dielectric function. The computational domain ranges from $n_e = 0.001 n_c$ to $n_e = 1 n_c$. Because SBS light is treated as a broadband signal in this model, its spectrum at a given moment can be obtained by solving the coupled Eqs. (1) and (2) based on the corresponding plasma parameters. Doing this calculation for the whole duration of the interaction beam, one then obtains the time-resolved SBS spectra.

As mentioned in Sec. I, the neglect of collisional damping in SBS calculations may overestimate the SBS growth in the Au plasma. Collisions in an ICF plasma include electron–electron, electron–ion, and ion–ion collisions, whose mean free paths are given by $\lambda_{ee} = v_{Te}\tau_{ee}$, $\lambda_{ei} = v_{Te}\tau_{ei}$, and $\lambda_{ii} = v_{Ti}\tau_{ii}$, respectively, where $v_{Te} = \sqrt{T_e/m_e}$ and $v_{Ti} = \sqrt{T_i/m_i}$ are the thermal velocities of

electrons and ions, respectively. τ_{ee}, τ_{ei}, and τ_{ii} are the corresponding collision times.[29] The collisional effects on the IAW depend on the parameter $k_I\lambda$, where λ denotes λ_{ee}, λ_{ei}, or λ_{ii} for the respective collisions. If the parameter $k_I\lambda$ is not much greater than 1, the collisions provide non-negligible damping on the IAW. We consider two typical hohlraum plasmas, namely, an Au plasma (with $n_e = 0.12n_c$, $T_e = 1400$ eV, $T_i = 1200$ eV, and $Z = 39$) and a CH (C_5H_{12}) plasma (with $n_e = 0.09n_c$, $T_e = 1200$ eV, $T_i = 1000$ eV, and $\bar{Z} = \sum_i Z_i^2 n_i / \sum_i Z_i n_i \approx 4.57$). The parameters $k_I\lambda$ for the Au and CH plasmas are shown in Table I. Here, the quantities for the CH plasma are calculated by treating it as a single-ion-species plasma with $\bar{Z} = 4.57$. For the electron–electron and electron–ion collisions, the parameters $k_I\lambda_{ee}$ and $k_I\lambda_{ei}$ are much greater than 1 in both the Au and CH plasmas. This means that these collisions are quite weak and have little effect on SBS. On the other hand, for the ion–ion collisions, $k_I\lambda_{ii}$ is much less than 1 in the Au plasma and not much greater than 1 in the CH plasma. Therefore, ion–ion collisional damping is considered in the following calculations of SBS. This is realized by correcting the ion susceptibility:[30]

$$\chi_i^c = \begin{cases} \dfrac{ZT_e}{T_i}\alpha^2\left(-\dfrac{1}{x_i^2} - \dfrac{5}{3x_i^4} + i\dfrac{10}{9}\dfrac{k_I\lambda_{ii}}{x_i^3}\right), & k_I\lambda_{ii} \le 0.1, \\ \dfrac{ZT_e}{T_i}\alpha^2\left(-\dfrac{1}{x_i^2} - \dfrac{11}{5}\dfrac{1}{x_i^4} + i\dfrac{16}{25}\dfrac{1}{k_I\lambda_{ii}x_i^5} + i\sqrt{\dfrac{\pi}{2}}x_i e^{-x_i^2/2}\right), & 0.1 < k_I\lambda_{ii} < 10, \\ \dfrac{ZT_e}{T_i}\alpha^2\left(-\dfrac{1}{x_i^2} - \dfrac{3}{x_i^4} + i\dfrac{8}{5}\dfrac{1}{k_I\lambda_{ii}x_i^5} + i\sqrt{\dfrac{\pi}{2}}x_i e^{-x_i^2/2}\right), & k_I\lambda_{ii} \ge 10, \end{cases} \tag{4}$$

TABLE I. Parameters $k_I\lambda$ for Au and CH plasmas.

	$k_I\lambda_{ii}$	$k_I\lambda_{ei}$	$k_I\lambda_{ee}$
Au	0.017	25	1413
CH	13.9	296	1916

where $\alpha = (k_I\lambda_D)^{-1}$, λ_D is the the electron Debye length, $x_i = \omega_I/k_I v_{Ti}$, and ω_I is the frequency of the IAW. This corrected ion susceptibility χ_i^c is then substituted into Eq. (3), to solve the coupled Eqs. (1) and (2).

To calculate the TS spectra, the electron density fluctuation δn_e of the IAW is required. In stimulated scattering, the electron density fluctuations are driven by the ponderomotive force, which can be described by the following equation:[19,31]

$$\delta n_e(k_I, \omega_I) = -\frac{1}{2}\frac{k_I^2 e^2 n_e}{m_e^2 c^2 \omega_{pe}^2}\frac{\chi_e(1+\chi_i^c)}{\varepsilon} a_0 a_s^*. \tag{5}$$

Here, ω_{pe} is the electron plasma frequency, and a_0 and a_s are respectively the complex envelopes of the pump laser (0) and the scattered light (s). The complex envelopes and laser intensities are related by $I_0 = v_{g0}\omega_0^2|a_0|^2/8\pi c^2$ for the interaction beam and $i_s\,\mathrm{d}\omega_s = v_{gs}\omega_s^2|a_s|^2/8\pi c^2$ for the SBS light within the frequency interval between ω_s and $\omega_s + \mathrm{d}\omega_s$, where v_{g0} and v_{gs} are respectively the group velocities of the interaction beam and the SBS light in the plasmas. The TS light (I_{TS}) off SBS-driven IAWs can be obtained from the electron density fluctuation:[32]

$$I_{\mathrm{TS}}(\vec{k}_{\mathrm{TS}}, \omega_{\mathrm{TS}}) = I_{\mathrm{pr}} r_e^2 \Delta\Omega \left\langle \int_V \mathrm{d}V\, \delta n_e(\vec{k}_I, \omega_I) \right\rangle^2 \times \propto [V\overline{\delta n}_e(\vec{k}_I, \omega_I)]^2. \tag{6}$$

Here I_{pr} is the intensity of the probe beam, $\Delta\Omega$ is the solid angle of the TS light, and V is the TS diagnostic volume. The wave vector and frequency of the TS light are $\vec{k}_{\mathrm{TS}} = \vec{k}_{\mathrm{pr}} \pm \vec{k}_I$ and $\omega_{\mathrm{TS}} = \omega_{\mathrm{pr}} \pm \omega_I$, respectively, where ω_{pr} is the frequency of the probe light and the sign $\pm$ depends on the specific geometric relationship. For a given moment, with the intensities of the interaction beam and SBS light in the diagnostic volume provided by the SBS calculation, the TS spectrum can be calculated by Eqs. (5) and (6). The time-resolved TS spectra are then obtained by doing the calculation for the whole duration of the probe beam.

V. CALCULATED RESULTS AND ANALYSIS

A. Influence of collisional damping on SBS

Figure 5 shows the spectra of SBS and TS calculated with ion–ion collisions either ignored or considered. The spectra from the ion–ion collisionless calculation [see Figs. 5(a) and 5(b)] reproduce the main features observed in the experiment [see Figs. 2(a) and 2(b)], with two components: one in an early phase during 0–0.6 ns and the other in a later phase during 1.2–1.9 ns. However, there is an extra strong signal during 0.5–1.5 ns with a wavelength shift of 0–0.2 nm, which was routinely seen in the previous calculations,[18] but was not measured in the experiment. The SBS spatial spectrum during 1.0 ns [Fig. 6(c)] clearly shows that the strong signal is from the Au plasma. In the collisionless case, the SBS growth rate in the Au plasma is larger than that in the CH plasma by one to two orders of magnitude [see Fig. 6(a)], and so SBS grows rapidly in the Au plasma, as shown in Fig. 6(c). In the calculated TS spectrum [Fig. 5(b)], there is also a strong TS signal near the 4ω during 0.5–1.5 ns, which demonstrates that a large-amplitude IAW is driven in the diagnostic volume by the pump laser and the SBS light from the Au plasma. When ion–ion collisions are considered, the spatial growth rate of SBS in the Au plasma broadens, with its peak value decreased by about an order of magnitude [see Fig. 6(b)]. As a result, the intensities of SBS light at the CH/Au interface and the left boundary both decrease by four orders of magnitude, as shown in Fig. 6(e). The SBS and TS spectra [see Figs. 5(c) and 5(d)] in this case basically

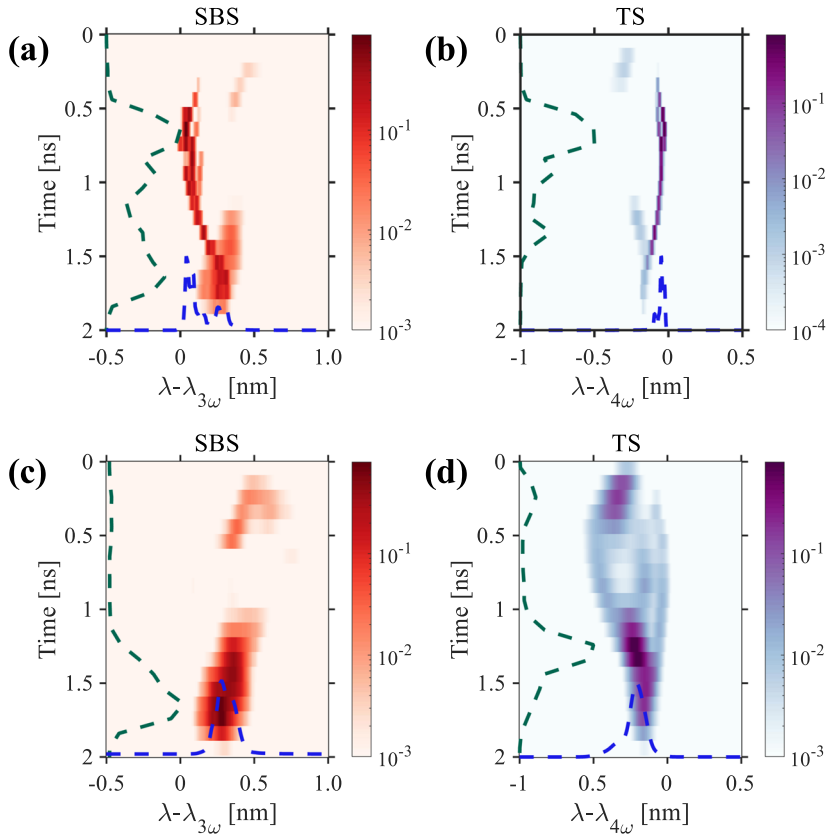

FIG. 5. Temporal spectra of SBS [(a) and (c)] and TS [(b) and (d)] light from calculations without [(a) and (b)] and with [(c) and (d)] ion–ion collisions.

agree with the experimental spectra, indicating that ion–ion collisions in the Au plasma may not be ignored in the analysis of SBS growth.

With ion–ion collision considered, the calculation [see Fig. 5(c)] shows that SBS is mainly from the late phase of the laser pulse (1.2–1.9 ns), weakly from the early phase (0–0.7 ns), and negligibly from the middle phase (0.7–1.2 ns). This behavior is primarily caused by the longitudinal (along the laser path) distributions of flow velocity and material (filled gas or covering membrane), as shown in Fig. 7(a) for three typical times (0.4, 1.0, and 1.6 ns). At 1.6 ns, the flow velocity is relatively uniform, which facilitates the growth of SBS; as a result, the SBS growth rate at this time is larger than those at the other two times, as shown in Fig. 7(b). Although the velocity gradient at 0.4 ns is greater than that at 1.0 ns, the former growth rate is larger than the latter. This is because the higher-Z membrane plasma at 0.4 ns makes a great contribution to the SBS growth, as can be seen by comparing the growth rates with (solid green line) and without (dashed green line) the membrane plasma in Fig. 7(b). This contribution is negligible at 1.0 and 1.6 ns, because the later flow velocity of the membrane plasma ($R < -600\ \mu$m) deviates from that of the interior plasma, causing the membrane plasma to decouple from the SBS light from the CH and Au plasmas.

Although the calculated SBS and TS spectra basically agree with the experimental results once ion–ion collisions have been considered, a quantitative discrepancy still exists. In the calculation, the early (0–0.7 ns) SBS light only accounts for 3% of the total SBS energy, whereas it accounts for 30% in the experiment. This discrepancy could result from two factors that are not well treated in the radiation-hydrodynamics simulation. First, the use of a mass-equivalent membrane in the simulation would lead to a lower membrane density than in the experiment, which may lead to underestimation of the SBS in the membrane plasma. Second, restricted by the cylindrical symmetry of the simulation, the focal spot of the interaction beam (of diameter 300 μm in the experiment) is set to be the same as that of the heater beams (of diameter 500 μm in the experiment). This may underestimate the density piled up at the edges of the laser channel caused by laser heating, which would then lead to an underestimation of SBS from the channel edge in the early phase. In the following subsections, we will discuss these two factors in detail.

B. SBS in the covering membrane plasma

The covering membrane has a much higher initial density than the filled gas. It can generate a high-density membrane plasma at the beginning of the pulse, which may lead to strong SBS. However, since the it is difficult to simulate ultrathin and high-density materials in LARED, a low-density membrane of equal mass is used. This

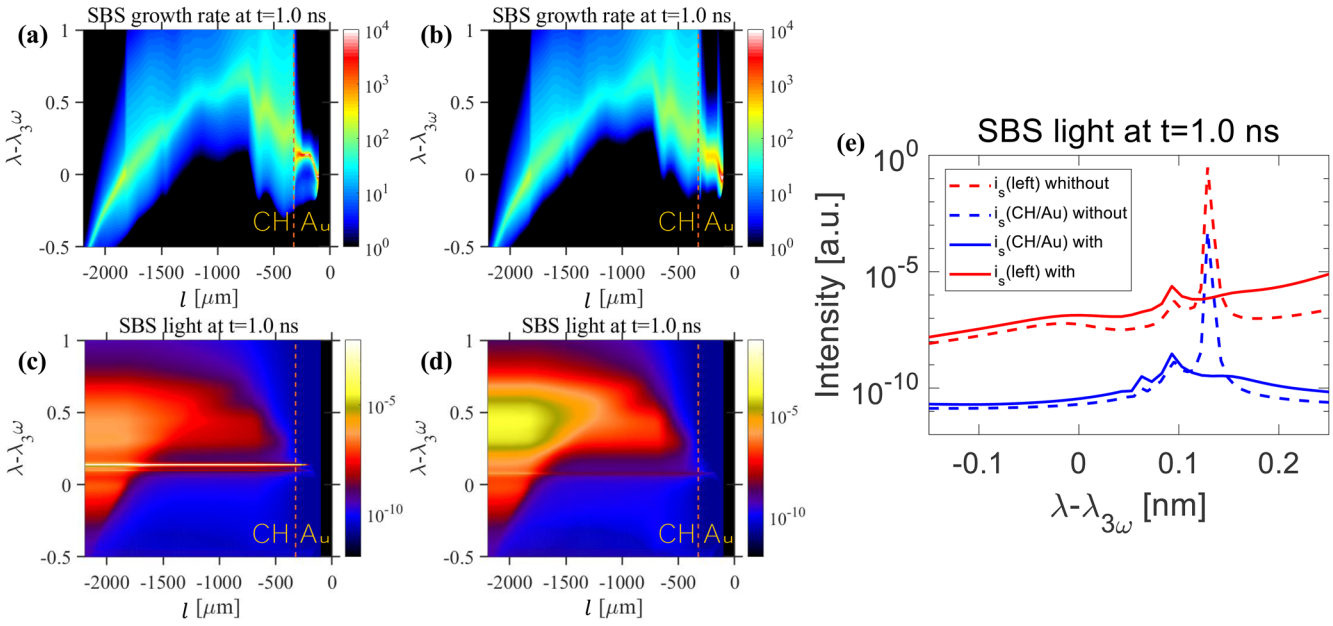

FIG. 6. Spatial growth rates [(a) and (b)] and spatial spectra [(c) and (d)] of SBS light from the calculations without [(a) and (c)] and with [(b) and (d)] ion–ion collisions, at 1.0 ns. The growth rates are calculated at the pump light intensity at the left boundary [$I_0(0)$] and the plasma length across the whole computational domain. (e) SBS spectra at (red lines) the left boundary and (blue lines) the CH/Au interface from the calculations without (dashed lines) and with (solid lines) ion–ion collisions.

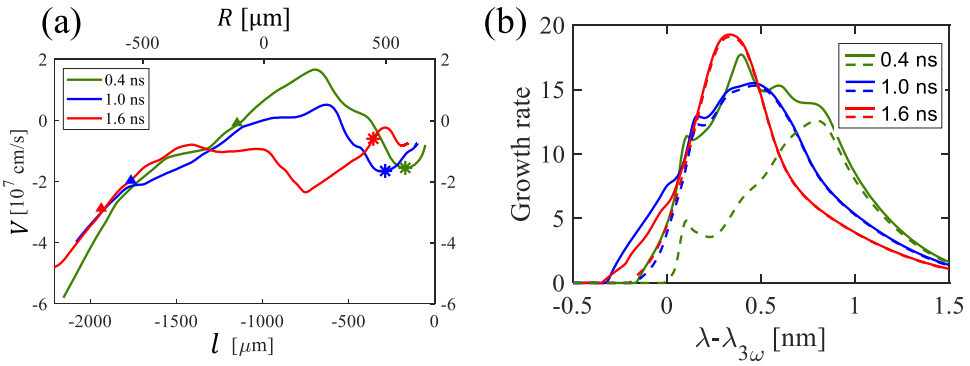

FIG. 7. (a) Profiles of plasma flow velocity along the ray path. The triangles and stars indicate the membrane/CH and CH/Au interfaces, respectively. (b) Spatial integral growth rates over the entire computational domain with (solid lines) and without (dashed lines) the membrane plasma.

treatment could lead to a low plasma density around the LEH and thus an underestimation of SBS at early times (0–0.7 ns). To examine this hypothesis, we calculate the SBS and TS spectra by doubling the membrane plasma density in 0–0.7 ns, as shown in Fig. 8. The higher-density in membrane plasma does produce stronger SBS light at early times, which makes the temporal behavior of SBS light closer to that in the experiment [green dashed lines in Figs. 2(a) and 8(a), respectively]. However, the early TS spectrum is almost completely suppressed as the membrane plasma density increases, which deviates from the experimental data [green dashed lines in Figs. 2(b) and 8(b), respectively]. According to the calculation, this suppression is caused by the pump depletion effect.[33] The stronger SBS in the membrane plasma around the LEH scatters more pump laser energy, leaving less energy arriving at the hohlraum interior; as a result, a weaker IAW is driven in the TS diagnostic volume, and hence weaker TS spectra are detected. As the membrane plasma density further increases, the deviation of the calculated early TS spectrum becomes greater. Therefore, the disagreement in the calculated and experimental TS spectra excludes the possibility that the relatively strong SBS in the early phase is from the dense membrane plasma.

C. Influence of transverse distribution of plasma parameters caused by laser heating

Laser heating leads to transverse plasma inhomogeneity, with the formation of a high-temperature, low-density plasma at the

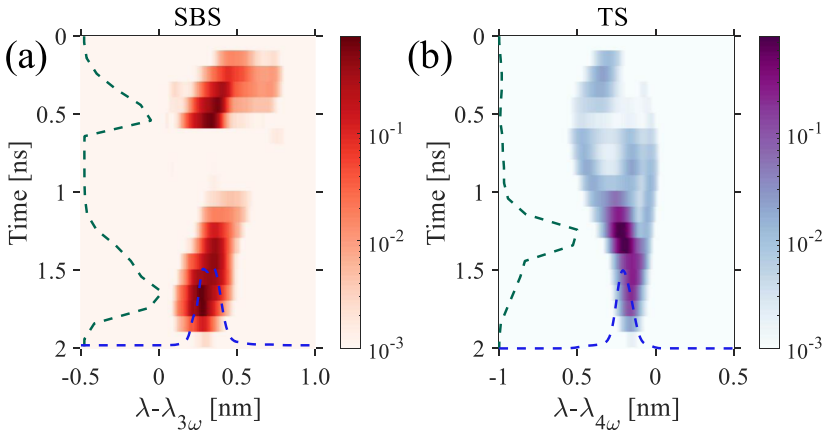

FIG. 8. Spectra of (a) SBS and (b) TS light calculated by doubling the membrane plasma density in 0–0.7 ns.

center of the laser channel and a low-temperature, high-density plasma at the edges and outside, similar to the features shown in Figs. 3 and 4. As stated above, the 300 μm-diameter interaction beam is replaced by a 500 μm-diameter beam in the radiation-hydrodynamics simulation. This difference in beam diameter will lead to an overestimation of the distance from the piled-up region to the beam axis and hence an underestimation of the density at the edges of the 300 μm-diameter interaction beam. On the other hand, in the SBS calculation, the interaction is limited to a region with a transverse size of 300 μm in diameter, so as to be consistent with the experiment. This means that as long as the original plasma parameters from the simulation are used in the SBS calculation, the interaction in the high-density piled-up region will be underestimated. Therefore, to better reproduce the experiment, the transverse distribution of the plasma parameters should be corrected. Similarly, the TS probe beam can also perturb the plasma, which should also be considered in the SBS calculations.

As shown in Fig. 4, owing to the plasma evolution, the transverse inhomogeneity of plasma parameters inside the laser channel lasts only for a short time interval. After $t = 0.7$ ns, the plasma becomes uniform. Hence, the correction of plasma parameters caused by the interaction beam only applies to the early phase (0–0.7 ns) in the following calculations. To quantitatively correct the plasma parameters, we use the energy deposition and transport model from Ref. 20. In this model, the energy deposited into the plasma by the inverse bremsstrahlung process and the energy lost from the plasma via the transverse electron thermal transport are in equilibrium. Thus, the electron temperature T_e satisfies the following equation:

$$\frac{\omega_{pe}^2}{\omega_0^2}\frac{\nu_{ei}}{\nu_{g0}} f_L f_{sc} I_0(r) = -\kappa_Q \frac{1}{r}\frac{\partial T_e(r)}{\partial r}, \tag{7}$$

where ν_{ei} is the electron–ion collision frequency, r is the distance from the beam axis, and f_L and f_{sc} are the Langdon absorption-reduction factor and ion screening correction factor, respectively, as given in Ref. 34. The local thermal conductivity is $\kappa_Q = \beta(\bar{Z}) n_e T_e / m_e \nu_{ei}$, where $\beta(\bar{Z})$ is a coefficient related to the average ion charge $\bar{Z}$,[35] given approximately by $\beta(\bar{Z}) = 3.2(0.24 + \bar{Z})/(1 + 0.24\bar{Z}) \simeq 7.34$. The electron density is considered to satisfy thermal pressure equilibrium, $n_e(0)T_e(0) = n_e(r)T_e(r) = \cdots = n_e(\infty)T_e(\infty)$. Since the f_L and f_{sc} depend on T_e, Eq. (7) has to be solved numerically. The boundary electron density $n_e(\infty)$ is set as the initially fully ionized electron density of the filled gas ($\sim 0.07 n_c$). The boundary electron temperature $T_e(\infty)$ is set as 0.4 keV, which is the electron temperature outside the laser channel at 0.2 ns from the LARED simulation.

Figure 9 shows the calculated transverse profiles of the electron temperature and density for two laser intensity profiles corresponding respectively to the interaction beam with a diameter of 300 μm and the heater beam with a diameter of 500 μm. The laser intensity profiles used here are tenth-order super-Gaussian distributions. As can be seen, at the edges of the interaction beam (gray region in Fig. 9), the plasma heated by the interaction beam has ~30% higher electron density and ~20% lower electron temperature than the plasma heated by the heater beam. These relative variations in electron density and temperature are applied to the simulated plasma parameters for correction.

In principle, the plasma flow should also be corrected when the smaller-size interaction beam is considered. However, this correction has a negligible impact on the SBS calculation for two reasons. First, the perturbation caused by the interaction beam is primarily along its transverse direction, whereas the 1D SBS calculation depends only on the plasma flow along the longitudinal direction. Second, the transverse perturbation quickly spreads out of the interaction beam channel. By contrast, the TS probe beam propagates across the interaction beam at an angle of 45°, and so its heating effect will lead to a correction of plasma parameters (including electron density, electron temperature, and plasma flow velocity) not only within the probe beam channel, but also along the interaction beam channel as the perturbation spreads. Consequently, this correction should be taken into account in the SBS calculation throughout the presence of the TS probe beam. In this case, the energy deposition and transport model used above is no longer applicable.

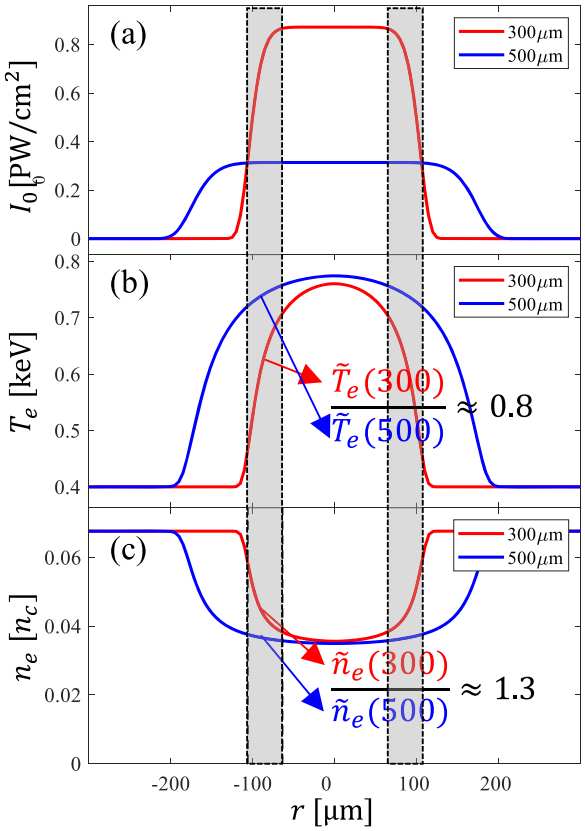

FIG. 9. Transverse profiles of (a) laser intensity, (b) electron temperature and (c) electron density for beams with different diameters: the interaction beam with a diameter of 300 μm (red) and the heater beam with a diameter of 500 μm in the LEH plane (blue).

To investigate the effect of the probe beam on the plasma parameters, a separate simulation is performed with LARED. In this simulation, a cup-shaped Au hohlraum with a diameter of 1 mm and a length of 1.5 mm is initially filled with pentane (C_5H_{12}) at a pressure of 0.6 atm. The initial electron temperature of the filled gas is set as 10 eV, which corresponds to the electron temperature outside the interaction beam at −0.1 ns in the above-mentioned simulation case. The probe beam with the same settings as the experiment (60 J energy, a 70 μm-diameter spot, and a 3 ns-square pulse) is injected into the hohlraum along its axis from the open end and terminates at the closed end, as shown in Fig. 10(a). As expected, the probe beam heats the nearby plasma to 0.3–0.4 keV, and also forms a density valley and density peaks at the center and the edges of the beam, respectively, as displayed in Figs. 10(b)–10(d). The density peak moves transversely outward at a speed of 1.2×10^7 cm/s. Along with the outward movement of the density peak, the local plasma flow is also perturbed. To take these impacts into account, the previously simulated electron density around the probe beam is corrected by multiplying by the normalized density profile $n_e(s,t)/n_0$ obtained here, and the plasma flow velocity and electron temperature along the transverse direction of the probe beam are corrected by adding the velocity $V(s,t)$ and temperature $T_e(s,t)$ obtained here. n_0 is the initial electron density, and s denotes the coordinate along the transverse direction of the probe beam, which corresponds to the direction along the hohlraum axis in the previous simulation. Unlike the correction resulting from the interaction beam, which works only in the early phase (0–0.7 ns), the correction resulting from the probe beam lasts for the whole interaction period (2 ns), because it continues to affect the SBS process.

The heating effects of the 300 μm-diameter interaction beam and the probe beam affect SBS by perturbing the flow velocity, temperature, and density. The longitudinal distributions of electron temperature and flow velocity with the corrections for the heating effect of the TS probe beam are shown in Fig. 11 (solid lines). As can be seen, compared with the uncorrected results (dashed lines), the plasma flow velocity is only weakly affected. Although the electron temperature near the probe beam ($-1200\ \mu\text{m} \le l \le -650\ \mu\text{m}$) rises slightly from 1.3 to 1.7 keV, this is not sufficient to have a noticeable effect on SBS. The temperature and velocity corrections caused by the probe beam will red-shift the SBS light by ~0.05 nm and attenuate it by ~5%. Similarly, the temperature drop caused by the interaction beam has a minor effect on SBS.

The interaction beam and probe beam affect SBS primarily by perturbing the electron density. Figure 12 shows the spatial distributions of electron density and SBS reflectivity with (solid lines) and without (dashed lines) the corrections due to the heating effect. The electron density at the edge of the interaction beam increases by ~30% [see Fig. 12(a), red lines] in the early phase (0–0.7 ns), resulting in the intensity of the SBS light at the left boundary rising by about an order of magnitude [see Fig. 12(a), blue lines]. The probe beam attenuates SBS by reducing the density near the diagnostic volume. In the early phase, the lengths of plasma affected by the probe beam are less than 350 μm, and so the impact on SBS is weak (~5% reduction in SBS intensity). As the perturbed region spreads out, more of the plasma is depressed, and the impact then becomes prominent. At 1.6 ns, the depressed region is ~600 μm along the interaction beam, and hence the SBS light at the left boundary is attenuated by ~65%, as shown in Fig. 12(b). The probe light reduces the average SBS reflectivity by about 50% within the interaction beam duration.

The corrections caused by the heating effects of the 300 μm-diameter interaction beam and the probe beam greatly affect the temporal behavior of the SBS, as shown in Fig. 13(a). The SBS light calculated based on the original simulated plasma parameters [blue line in Fig. 13(a)] mainly appears in the late phase of the pulse, with negligible signal in the early phase, which is quite different from the experimental result [black line in Fig. 13(a)]. The calculated average SBS reflectivity in this case is 6%, which is also larger than the experimental result (~4%). After considering the correction (mainly density increases at the channel edges) caused by the 300 μm-spot interaction beam, the early SBS light grows to an appreciable intensity [green line in Fig. 13(a)], and the SBS reflectivity raises to ~7%. The additional perturbation (mainly density drop) caused by the probe beam then attenuates the late SBS, resulting in comparable intensities of early and late SBS, and a smaller overall reflectivity of ~3%, as shown by the red line in Fig. 13(a). With these corrections, the calculated SBS spectrum [see Fig. 13(c)] agrees very well with the experimental result [see Fig. 2(a)].

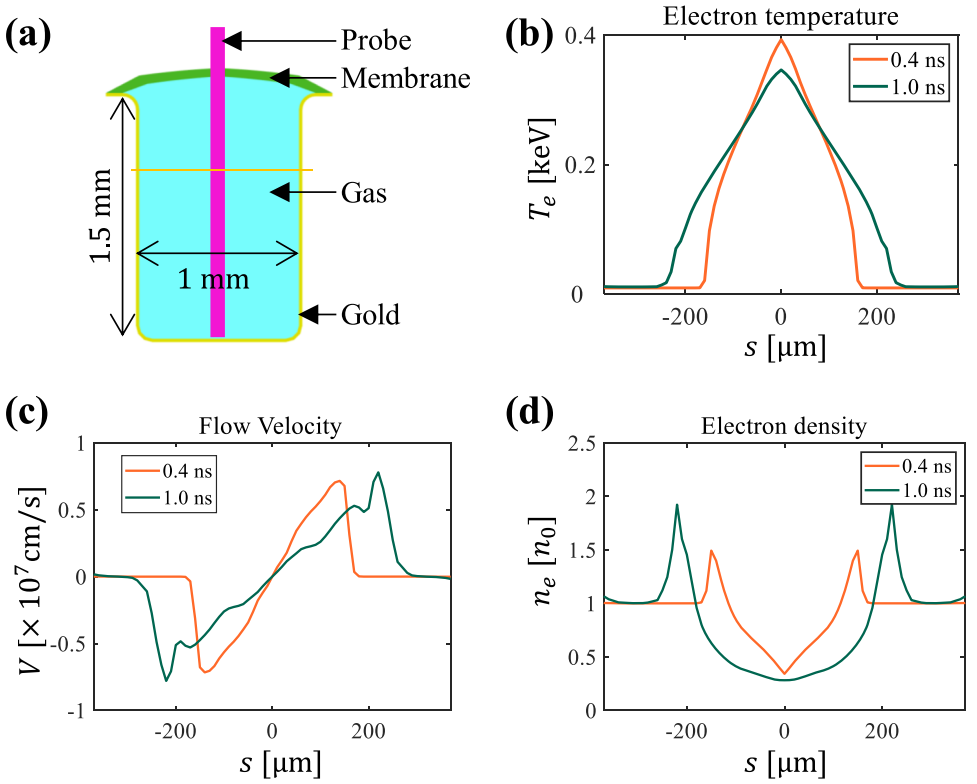

FIG. 10. (a) Schematic of the simulation for a cup-shaped hohlraum. (b)–(d) Distributions of electron temperature, flow velocity, and electron density, respectively, at 0.4 ns (orange lines) and 1.0 ns (dark green lines) along the transverse direction of the probe beam [on the yellow line in (a)]. n_0 here denotes the initial electron density.

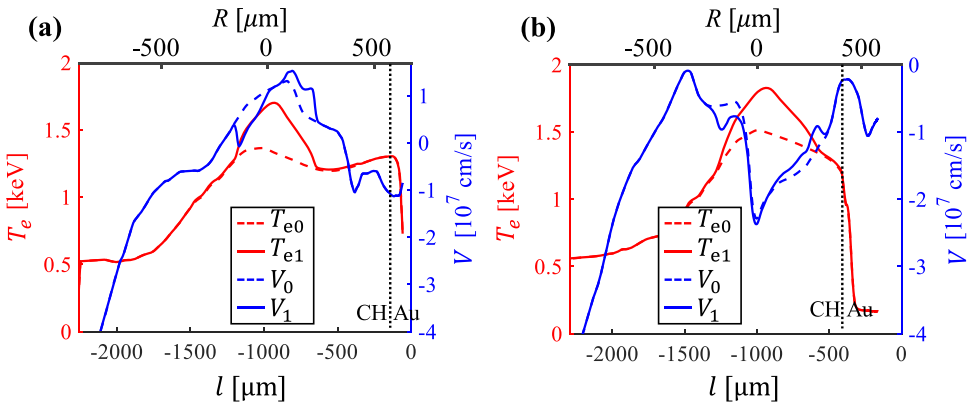

FIG. 11. Spatial distributions of electron temperature (red lines) and plasma flow velocity (blue lines) along the interaction beam at (a) 0.4 ns and (b) 1.6 ns. The dashed lines show the original data from the LARED simulation, and the solid lines are the results corrected by considering the heating effect of the TS probe beam.

The calculated TS spectrum [see Fig. 13(d)] is also favorably consistent with the experimental result. Since the TS diagnostic volume is at the center of the interaction beam channel, the TS spectrum is not affected by the plasma parameter correction at the channel edges caused by the heating effect of the interaction beam. As a result, when the heating effect of the interaction beam is considered, the temporal behavior of the TS light [case B, green line in Fig. 13(b)] is identical with that from the uncorrected calculation case (case A, blue line). The electron density drop near the TS diagnostic volume caused by the probe beam reduces the amplitude of the SBS-driven IAW, leading to reductions in the intensity of TS light by ~35% in the early phase (0–0.7 ns) and by ~50% in the late

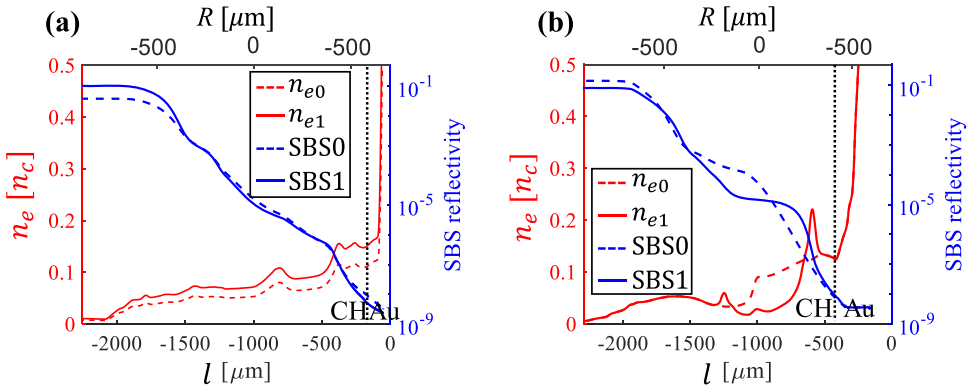

FIG. 12. Spatial distributions of electron density (red lines) and SBS reflectivity (blue lines) along the edge of the interaction beam near the hohlraum center. The dashed lines show the original data from the LARED simulation, and the solid lines are the results after considering the heating effects of (a) the 300 μm-diameter interaction beam at 0.4 ns and (b) the TS probe beam at 1.6 ns.

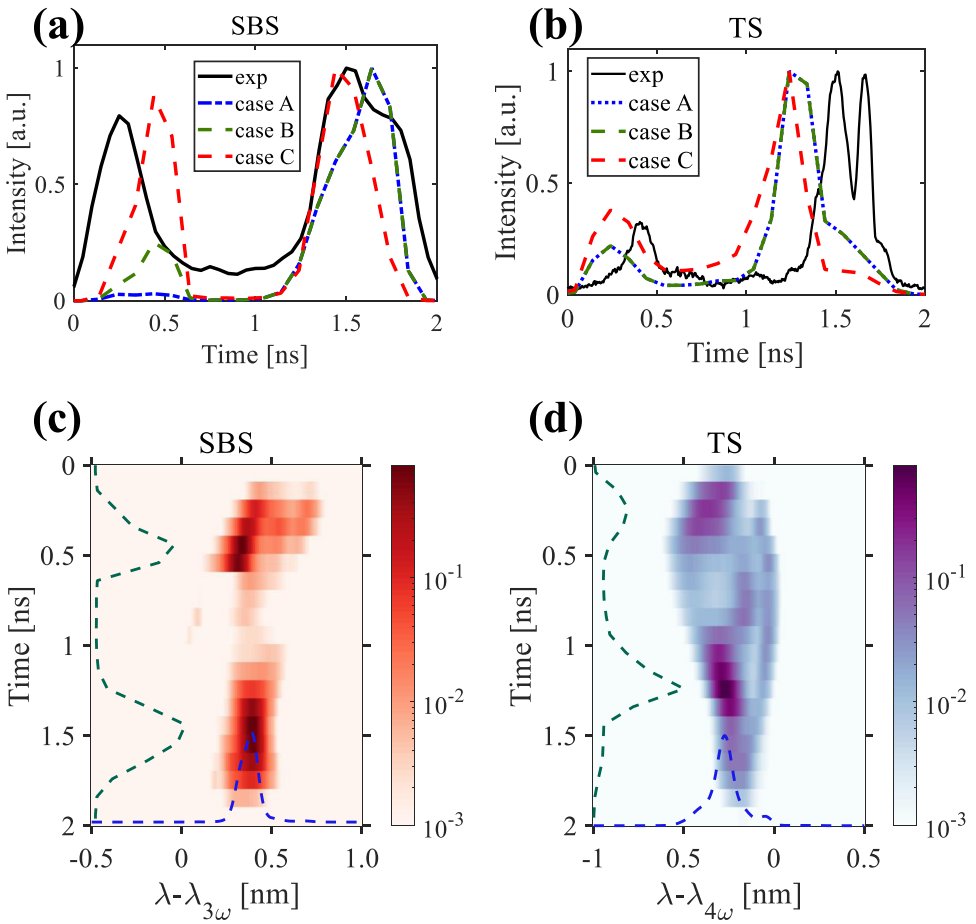

FIG. 13. (a) and (b) Temporal behaviors of SBS and TS light, respectively. Here, the black lines are experimental data. The colored lines represent three calculation cases: case A (blue) is the calculation with the original simulated plasma parameters; case B (green) is the calculation considering only the heating effect of the interaction beam; case C (red) is the calculation considering the heating effects of both the interaction beam and the TS probe beam. (c) and (d) Spectra of SBS and TS light, respectively, from calculation case C.

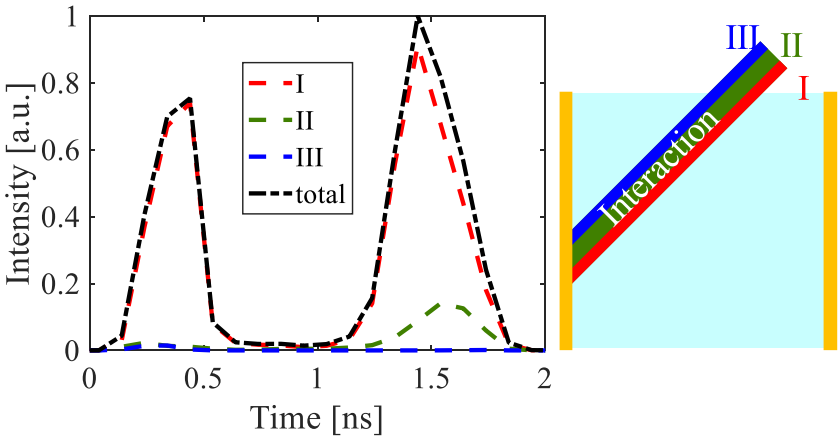

FIG. 14. Temporal behavior of SBS lights from different regions of the interaction beam: upper edge (blue), central region (green), lower edge (red), and whole beam (black).

phase (1.2–1.9 ns), respectively. Consequently, the contrast between the early and late components decreases, as shown by the red line in Fig. 13(b), which agrees better with the experimental result (black line).

The calculations also reveal a significant difference between the SBS light from the edges and from the center of the interaction beam, as shown in Fig. 14. The SBS light at the lower edge of the interaction beam (region I, red in Fig. 14) contributes ~92% to the total energy, and ~100% in the early component (0–0.7 ns). The SBS light near the center of the interaction beam (region II, green in Fig. 14) contributes ~8% to the total energy, and ~13% to the late component (1.2–1.9 ns). The SBS light at the upper edge of the interaction beam (region III, blue in Fig. 14) is very weak, contributing less than 1% to the total SBS energy. Such different contributions are primarily due to effective plasma lengths (with $0.01n_c \le n_e < 1n_c$) and electron densities in the different regions. The effective plasma lengths of the three regions are respectively 2040 μm (I), 1890 μm (II), and 1720 μm (III). At 1.6 ns, the average electron densities in regions I, II, and III are $0.093n_c$, $0.065n_c$ and $0.040n_c$, respectively. The high density in region I is a result of compression around the hohlraum axis caused by the expansion of the hohlraum wall, while the low density in region III is due to rarefaction around the LEH caused by the outward flow.

It should be noted that the ion trapping effect is not taken into account in the analysis, because it is not an important factor here. For the typical parameters in our experiment, the threshold for ion trapping to cause SBS saturation is $n_{\rm th}/n_e \sim 2.5\%$,[23,36] whereas in the calculations, even at the moment with the strongest SBS, the IAW amplitude $\delta n_e/n_e$ is less than 1.5%. Therefore, the ion trapping effect may not lead to SBS saturation, and neglecting it is acceptable.

VI. CONCLUSIONS

The TS technique has been used in a gas-filled hohlraum for the first time to study the spatial growth of SBS by detecting the SBS-driven IAW. The time-resolved SBS and TS spectra obtained in the experiment have been analyzed with a steady-state code based on a ray-tracing model. The analysis indicates that ion–ion collisions may play an important role in suppressing SBS growth in the Au plasma, as a result of which the SBS excited in the gas-filled region dominates. In the early phase of the main pulse (0–0.7 ns), the heating effect of the interaction beam piles up plasma at its channel edges, which could be responsible to the early strong SBS. In the middle phase (0.7–1.2 ns), SBS is detuned by inhomogeneity of the plasma flow velocity, resulting in a negligible contribution. In the late phase (1.2–1.9 ns), the plasma flow velocity along the interaction beam is relatively uniform, which facilitates the growth of SBS. The presence of the TS probe beam in the experiment might mitigate SBS by perturbing the density distribution around the region overlapping with the interaction beam. This impact increases as the perturbed region spreads with time. The results of the experiment and analysis presented in this work will help comprehension of the SBS growth in gas-filled hohlraums, and could be valuable for future ignition target design.

ACKNOWLEDGMENTS

This work is supported by the Natural Science Foundation of China (Grant Nos. 11905204, 11975215, 12105270, 12205272, 12205274, 12275032, 12275251, and 12035002), and the Laser Fusion Research Center Funds for Young Talents (Grant No. RCFPD3-2019-6).

AUTHOR DECLARATIONS

Conflict of Interest

The authors have no conflicts to disclose.

Author Contributions

Chaoxin Chen: Formal analysis (equal); Investigation (equal); Methodology (equal); Writing – original draft (equal). **Tao Gong**: Conceptualization (equal); Investigation (equal); Writing –

review & editing (equal). **Zhichao Li**: Conceptualization (supporting); Investigation (supporting); Project administration (supporting); Supervision (equal). **Liang Hao**: Investigation (equal); Software (lead). **Yonggang Liu**: Investigation (supporting). **Xiangming Liu**: Investigation (supporting). **Hang Zhao**: Investigation (supporting). **Yaoyuan Liu**: Investigation (supporting). **Kaiqiang Pan**: Investigation (supporting). **Qi Li**: Investigation (supporting). **Sanwei Li**: Investigation (supporting); Supervision (supporting). **Zhijun Li**: Investigation (equal). **Sai Jin**: Investigation (equal). **Feng Wang**: Project administration (lead); Resources (lead); Supervision (lead). **Dong Yang**: Funding acquisition (lead); Project administration (equal); Supervision (supporting).

DATA AVAILABILITY

The data that support the findings of this study are available from the corresponding author upon reasonable request.

REFERENCES

[1] J. D. Lindl, P. Amendt, R. L. Berger, S. G. Glendinning, S. H. Glenzer, S. W. Haan, R. L. Kauffman, O. L. Landen, and L. J. Suter, "The physics basis for ignition using indirect-drive targets on the National Ignition Facility," Phys. Plasmas **11**, 339–491 (2004).

[2] W. Kruer, *The Physics of Laser Plasma Interactions* (CRC Press, 2019).

[3] J. Ralph, A. Kemp, N. Meezan, R. Berger, D. Strozzi, B. MacGowan, O. Landen, N. Lemos, M. Belyaev, M. Biener *et al.*, "The effects of multispecies hohlraum walls on stimulated brillouin scattering, hohlraum dynamics, and beam propagation," Phys. Plasmas **28**, 072704 (2021).

[4] G. Hall, O. Jones, D. Strozzi, J. Moody, D. Turnbull, J. Ralph, P. Michel, M. Hohenberger, A. Moore, O. Landen *et al.*, "The relationship between gas fill density and hohlraum drive performance at the National Ignition Facility," Phys. Plasmas **24**, 052706 (2017).

[5] R. Berger, C. A. Thomas, K. Baker, D. Casey, C. Goyon, J. Park, N. Lemos, S. Khan, M. Hohenberger, J. Milovich *et al.*, "Stimulated backscatter of laser light from BigFoot hohlraums on the National Ignition Facility," Phys. Plasmas **26**, 012709 (2019).

[6] T. Chapman, P. Michel, J.-M. Di Nicola, R. Berger, P. Whitman, J. Moody, K. Manes, M. Spaeth, M. Belyaev, C. Thomas, and B. J. MacGowan, "Investigation and modeling of optics damage in high-power laser systems caused by light backscattered in plasma at the target," J. Appl. Phys. **125**, 033101 (2019).

[7] H. Abu-Shawareb, R. Acree, P. Adams, J. Adams, B. Addis, R. Aden, P. Adrian, B. Afeyan, M. Aggleton, L. Aghaian *et al.*, "Lawson criterion for ignition exceeded in an inertial fusion experiment," Phys. Rev. Lett. **129**, 075001 (2022).

[8] A. Kritcher, A. Zylstra, D. Callahan, O. Hurricane, C. Weber, J. Ralph, D. Casey, A. Pak, K. Baker, B. Bachmann *et al.*, "Achieving record hot spot energies with large HDC implosions on NIF in HYBRID-E," Phys. Plasmas **28**, 072706 (2021).

[9] S. Haan, J. Lindl, D. Callahan, D. Clark, J. Salmonson, B. Hammel, L. Atherton, R. Cook, M. Edwards, S. Glenzer *et al.*, "Point design targets, specifications, and requirements for the 2010 ignition campaign on the National Ignition Facility," Phys. Plasmas **18**, 051001 (2011).

[10] M. Edwards, P. Patel, J. Lindl, L. Atherton, S. Glenzer, S. Haan, J. Kilkenny, O. Landen, E. Moses, A. Nikroo *et al.*, "Progress towards ignition on the National Ignition Facility," Phys. Plasmas **20**, 070501 (2013).

[11] T. Dittrich, O. Hurricane, D. Callahan, E. Dewald, T. Döppner, D. Hinkel, L. Berzak Hopkins, S. Le Pape, T. Ma, J. Milovich *et al.*, "Design of a high-foot high-adiabat ICF capsule for the National Ignition Facility," Phys. Rev. Lett. **112**, 055002 (2014).

[12] R. Kirkwood, J. Moody, J. Kline, E. Dewald, S. Glenzer, L. Divol, P. Michel, D. Hinkel, R. Berger, E. Williams *et al.*, "A review of laser–plasma interaction physics of indirect-drive fusion," Plasma Phys. Controlled Fusion **55**, 103001 (2013).

[13] S. Glenzer, L. Divol, R. Berger, C. Geddes, R. Kirkwood, J. Moody, E. Williams, and P. Young, "Thomson scattering measurements of saturated ion waves in laser fusion plasmas," Phys. Rev. Lett. **86**, 2565 (2001).

[14] P. Masson-Laborde, M. Monteil, V. Tassin, F. Philippe, P. Gauthier, A. Casner, S. Depierreux, C. Neuville, B. Villette, S. Laffite *et al.*, "Laser plasma interaction on rugby hohlraum on the Omega Laser Facility: Comparisons between cylinder, rugby, and elliptical hohlraums," Phys. Plasmas **23**, 022703 (2016).

[15] N. Meezan, L. Atherton, D. Callahan, E. Dewald, S. Dixit, E. Dzenitis, M. Edwards, C. Haynam, D. Hinkel, O. Jones *et al.*, "National Ignition Campaign Hohlraum energetics," Phys. Plasmas **17**, 056304 (2010).

[16] T. Gong, L. Hao, Z. Li, D. Yang, S. Li, X. Li, L. Guo, S. Zou, Y. Liu, X. Jiang *et al.*, "Recent research progress of laser plasma interactions in Shenguang laser facilities," Matter Radiat. Extremes **4**, 055202 (2019).

[17] D. Strozzi, E. Williams, D. Hinkel, D. Froula, R. London, and D. Callahan, "Ray-based calculations of backscatter in laser fusion targets," Phys. Plasmas **15**, 102703 (2008).

[18] L. Hao, Y. Zhao, D. Yang, Z. Liu, X. Hu, C. Zheng, S. Zou, F. Wang, X. Peng, Z. Li *et al.*, "Analysis of stimulated Raman backscatter and stimulated Brillouin backscatter in experiments performed on SG-III prototype facility with a spectral analysis code," Phys. Plasmas **21**, 072705 (2014).

[19] T. Gong, Z. Li, B. Zhao, G.-y. Hu, and J. Zheng, "Noise sources and competition between stimulated Brillouin and Raman scattering: A one-dimensional steady-state approach," Phys. Plasmas **20**, 092702 (2013).

[20] T. Gong, J. Zheng, Z. Li, Y. Ding, D. Yang, G. Hu, and B. Zhao, "Mitigating stimulated scattering processes in gas-filled hohlraums via external magnetic fields," Phys. Plasmas **22**, 092706 (2015).

[21] L. Hao, D. Yang, X. Li, Z. Li, Y. Liu, H. Cai, Z. Liu, P. Gu, T. Xu, S. Li *et al.*, "Investigation on laser plasma instability of the outer ring beams on SGIII laser facility," AIP Adv. **9**, 095201 (2019).

[22] D. H. Froula, *Plasma Scattering of Electromagnetic Radiation* (Academic Press is an imprint of Elsevier, 2011), p. 8.

[23] D. Froula, L. Divol, and S. Glenzer, "Measurements of nonlinear growth of ion-acoustic waves in two-ion-species plasmas with Thomson scattering," Phys. Rev. Lett. **88**, 105003 (2002).

[24] D. Froula, L. Divol, A. MacKinnon, G. Gregori, and S. Glenzer, "Direct observation of stimulated-Brillouin-scattering detuning by a velocity gradient," Phys. Rev. Lett. **90**, 155003 (2003).

[25] H. Bandulet, C. Labaune, K. Lewis, and S. Depierreux, "Thomson-scattering study of the subharmonic decay of ion-acoustic waves driven by the Brillouin instability," Phys. Rev. Lett. **93**, 035002 (2004).

[26] C. Chen, T. Gong, Z. Li, H. Zhao, D. Yang, X. Jiang, Y. Liu, Z. Li, S. Jin, R. Zhao *et al.*, "Implementation of a large-aperture Thomson scattering system for diagnosing driven ion acoustic waves on Shenguang-III prototype laser facility," J. Instrum. **17**, P05017 (2022).

[27] H. Yong, P. Song, C.-L. Zhai, D.-G. Kang, J.-F. Gu, X.-D. Hang, P.-J. Gu, and S. Jiang, "Numerical simulation of 2-D radiation-drive ignition implosion process," Commun. Theor. Phys. **59**, 737 (2013).

[28] H. Zhao, Z. Li, D. Yang, X. Li, Y. Chen, X. Jiang, Y. Liu, T. Gong, L. Guo, S. Li *et al.*, "Progress in optical Thomson scattering diagnostics for ICF gas-filled hohlraums," Matter Radiat. Extremes **4**, 055201 (2019).

[29] F. L. Hinton, "Collisional transport in plasma," in *Handbook of Plasma Physics*, edited by A. A. Galeev and R. N. Sudan (North-Holland Publishing Company, 1983), p. 158.

[30] J. Zheng, C. Yu, and Z. Zheng, "The dynamic form factor for ion-collisional plasmas," Phys. Plasmas **6**, 435–443 (1999).

[31] J. F. Drake, P. K. Kaw, Y.-C. Lee, G. Schmid, C. S. Liu, and M. N. Rosenbluth, "Parametric instabilities of electromagnetic waves in plasmas," Phys. Fluids **17**, 778–785 (1974).

[32] D. Froula, L. Divol, D. Braun, B. Cohen, G. Gregori, A. Mackinnon, E. Williams, S. Glenzer, H. Baldis, D. Montgomery, and R. P. Johnson, "Stimulated Brillouin scattering in the saturated regime," Phys. Plasmas **10**, 1846–1853 (2003).

[33]C. Tang, "Saturation and spectral characteristics of the Stokes emission in the stimulated Brillouin process," J. Appl. Phys. **37**, 2945–2955 (1966).
[34]D. Turnbull, J. Katz, M. Sherlock, L. Divol, N. Shaffer, D. Strozzi, A. Colaïtis, D. Edgell, R. Follett, K. McMillen *et al.*, "Inverse bremsstrahlung absorption," Phys. Rev. Lett. **130**, 145103 (2023).
[35]K. Molvig, A. N. Simakov, and E. L. Vold, "Classical transport equations for burning gas-metal plasmas," Phys. Plasmas **21**, 092709 (2014).
[36]D. Froula, L. Divol, A. Offenberger, N. Meezan, T. Ao, G. Gregori, C. Niemann, D. Price, C. Smith, and S. Glenzer, "Direct observation of the saturation of stimulated Brillouin scattering by ion-trapping-induced frequency shifts," Phys. Rev. Lett. **93**, 035001 (2004).